Full length article

Microstructural characterisation of metallic shot peened and laser shock peened Ti–6Al–4V

Steven J. Lainé [a, *], Kevin M. Knowles [a], Phillip J. Doorbar [b], Richard D. Cutts [b], David Rugg [b]

[a] Department of Materials Science and Metallurgy, Rolls-Royce University Technology Centre, University of Cambridge, 27 Charles Babbage Road, Cambridge, CB3 0FS, UK
[b] Rolls-Royce plc, PO Box 31, Derby, DE24 8BJ, UK

ABSTRACT

A detailed analysis has been conducted of Ti–6Al–4V processed by metallic shot peening and laser shock peening. Analysis by incremental hole drilling, electron backscattered diffraction microscopy, transmission electron microscopy and transmission Kikuchi diffraction microscopy is evaluated and discussed. The results of this analysis highlight the very different dislocation structures in surfaces processed by these two techniques. Transmission Kikuchi diffraction also has been used to evaluate sub-grains generated by laser shock peening. A notable feature of material processed by laser shock peening is the almost complete absence of deformation twinning, contrasting with the frequent observation of extensive deformation twinning observed in the material processed by metallic shot peening.

1. Introduction

Shot peening standards have existed for the aerospace industry since 1948 [1]. Titanium alloys with shot peened compressive residual stress at the surface of the components have been used extensively and successfully in the aerospace industry since the 1970s [2]. The use of shot peening as a method of mechanical prestressing originated from a recognition that metals shot blasted and cleaned with metallic shot exhibited improved strength [3]. The development of the 'Cloudburst Machine' machine by Herbert is recognised as the first shot peening machine in 1927 [3–5]. Almen filed the first shot blasting patent in 1944 [6,7]. By the 1960s shot peening was being used extensively in industry [8]. Cary, Hawkinson, Almen et al. and Champaigne provide informative and thorough histories of mechanical prestressing by shot peening [3,9–11]. Today, the conventional method of inducing the residual stress is by metallic shot peening (MSP), which provides residual stresses to a maximum depth of approximately 250 μm [12,13]. However, since around 2002 the aerospace industry and other industries with high cost components have also been applying laser shock peening (LSP) to increase the depth of the applied residual

stress. LSP is a well-established and commercially available process to induce deep residual surface stresses to millimetre depths on a wide variety of components including titanium alloy aerospace parts [12–16]. The technique adopts a high energy density, very short duration laser pulse to produce compressive loading in the surface of the metal. The shock loading is achieved via ablation of a coating or tape that is applied to the surface. The efficiency of the process may be enhanced with a transparent fluid layer for momentum transfer. The strain rate during LSP is estimated to be in excess of 10^6 s^{-1} [16–18].

The aim of the work discussed in this paper is to characterise the microstructures produced by mechanical prestressing in fine grained Ti–6Al–4V (wt. %) fan blade plate material by MSP and LSP. Although MSP and LSP are used extensively in the aerospace industry there is a lack of knowledge on the effects that the two methods have on the microstructure of titanium alloys, particularly relating to the levels of deformation twinning caused by the two techniques. Some authors have reported crystallographic features such as nanoscale grain recrystallisation and extremely thin nanoscale deformation twins in the surface layer of materials subjected to LSP surface treatment [18,19]. The transmission electron microscopy (TEM) results presented in this work investigate the nanoscale crystallographic effects of both MSP and LSP.

With the recent advances in electron backscattered diffraction

* Corresponding author.
  E-mail address: sl655@cam.ac.uk (S.J. Lainé).

(EBSD) acquisition time and EBSD pattern resolution, it is feasible to collect EBSD data from larger surfaces areas than are usually considered conventional to be collected by EBSD. For the work reported here, relatively large area scans have been constructed by stage driven montages of smaller maps that are stitched together. These large areas enable results that are more representative of the bulk material to be collected by EBSD. The EBSD results provide a measurement of the depth of deformation twinning and characterisation of deformation twinning type by analysis of the angle/axis pair relationships between the deformation twins and the parent grain. The potential modes of deformation twinning for hexagonal close packed (h.c.p.) titanium are summarised in Table 1 of Lainé and Knowles [20]. Grain orientation spread (GOS) and local misorientation measurements methods can also be used to quantify the extent of misorientation within grains in EBSD data [21,22]. The misorientation within grains is related to the dislocation density. Therefore, the extent of deformation can be inferred from the GOS measurement to estimate the depth of the residual stress layer produced by the residual stress technique. In this context, it is noteworthy that work by Child et al. on the nickel-based superalloy, Udimet$^©$ alloy 720Li, found that measuring the residual stress in EBSD scans with GOS measurements underestimated the depth as being approximately half the true depth [21].

There are two established methods of residual stress measurement that have been standardised by accompanying ASTM standards: incremental hole drilling [23] and X-ray diffraction using the $\sin^2 \psi$ method [24,25]. Incremental hole drilling is a destructive residual stress measurement [26–28]. A subsurface residual stress profile is obtained by first bonding a strain gauge rosette to the surface of the specimen. A small drilling rig is then used to drill a blind, flat bottomed hole and remove material at incremental depths in the centre of the strain gauge rosette. With each incremental depth of material that is removed from the hole, a change in the strain field takes place due to the relaxation of the surrounding material. The change in strain is measured by the strain gauges and the relaxation can be correlated with the residual stress that existed in the surface of the material. X-ray diffraction $\sin^2 \psi$ analysis is a non-destructive residual stress measurement. However, the penetration depth of laboratory-based Cu K$_\alpha$ X-ray systems is very low for metals, so that the diffracted beam only interacts with the top layer of the metal [29,30]. This means that measuring a depth profile requires an iterative process of material removal by electrolytic etching and X-ray measurements. The residual stress is quantified by measuring the lattice d spacing of specific planes (usually the $\{21\bar{3}3\}$ planes for titanium) and the plastic strain can be quantified by measuring the line broadening [30].

Although this method has the advantage of being able to measure inelastic strain, the incremental hole drilling method is considered to be a more accurate method of material removal for depth profiles [29]. Therefore, in our work, the residual stress measurements determined from EBSD GOS analysis have been compared to residual stress results obtained by the incremental hole drilling technique.

2. Experimental details

Samples of cross-rolled Ti–6Al–4V fan blade plate material were mill machined to the final geometry and then processed by MSP, LSP and a combination of both techniques. The microstructure of the Ti–6Al–4V samples was consistent with cross-rolled Ti–6Al–4V fan blade plate, with a fine polycrystalline primary α_p-phase (hexagonal close packed crystal structure) grain size of 10 μm–20 μm, with colonies of fine secondary α_s-phase laths with nanometre thicknesses of retained β-phase (body centred cubic

crystal structure) between the α_p-phase grains and α_s-phase laths. The MSP was conducted at an Almen intensity of between 6 A and 10 A according to standard SAE-J442 [31]. This means that an A-strip type Almen strip must deflect by between 0.15 mm and 0.25 mm after peening from one side only. An A-strip is a piece of spring steel with a through thickness of 0.129 mm (with a tolerance of ±0.02 mm), a length of 76.2 mm and a width of 19.05 mm. The shot type used was size 230 according to standard SAE-AMS-2431/1 [32]. This is cast steel shot with a diameter of 0.584 mm that has a hardness between 45 HRC (Rockwell hardness) and 52 HRC. LSP was conducted according to standard procedures for Ti–6Al–4V with a wavelength of 1054 nm, pulse durations of approximately 10 ns, an energy density of approximately 5 GW cm^{-2}, aluminium foil ablative coating and water overlay [16].

For convenience, the three samples will be referred to as MSP, LSP and LSP + MSP. The order corresponds to the sequence in which they are conducted with LSP being conducted prior to MSP. Incremental hole drilling, conducted by Stresscraft Ltd., was used to measure semi-destructively the sub-surface residual stress profiles generated by the two techniques. The limitations of the incremental hole drilling technique impose a tolerance of ±7% on the quoted values of residual stress.

EBSD data has been collected from millimetre-scale regions of the sectioned surfaces to ensure that the results are as statistically representative of bulk material as possible. The EBSD samples were prepared using the standard procedures for titanium and titanium alloys [33]. In order to remove strained material from the mechanical polishing stage the samples were first polished on a chemical resistant cloth using colloidal silica with an addition of 2% hydrogen peroxide H_2O_2 and 2% ammonia NH_3, with a subsequent vibratory polish in colloidal silica for 12–24 h used as a final stage in the metallographic polishing process. EBSD scans were conducted at 25 kV using a Schottky field emission gun (sFEG) source with a Phillips XL30 sFEG scanning electron microscope running the Oxford Instruments Aztec EBSD acquisition system. Transmission Kikuchi diffraction (TKD) EBSD scans was conducted at 30 kV on the same scanning electron microscope in transmission mode. The EBSD data were analysed using the HKL Channel 5 software package distributed by Oxford Instruments.

TEM analysis was also performed to assess the dislocation structures and deformation twinning present beneath the processed surface. Conventional TEM foil samples were prepared using electrical discharge machining to extract 3 mm diameter cylinders of material normal to the processed surfaces. The 3 mm cylinders were then cut into slices representing known depths into the processed surface. The slices of material were thinned to electron transparency using twin jet electropolishing following the standard procedures for titanium alloys in a solution of 10% perchloric acid $HClO_4$ in ethanol CH_3CH_2OH at −30 °C to minimise hydrogen diffusion into the samples [34,35]. Electropolished samples were thinned further by precision ion polishing in a Gatan PIPS II system. In addition focused ion beam (FIB) extraction has been used as a method of TEM foil preparation from specific regions of the samples. TEM FIB samples were prepared using a FEI Helios Nano Lab Dual Beam FIB SEM and analysed using either a JEOL 200CX or a Phillips CM30 transmission electron microscope at 200 kV equipped with a double tilt holder.

The specimens analysed by EBSD and TEM were sectioned from four point bend specimens as shown in Fig. 1(a). Incremental hole drilling results were taken from the same four point bend specimens, as shown in Fig. 1(b). However, because of the destructive nature of incremental hole drilling and the metallographic sectioning for EBSD, an equivalent position on the processed surface was analysed for comparison with EBSD, as shown in Fig. 1(a).
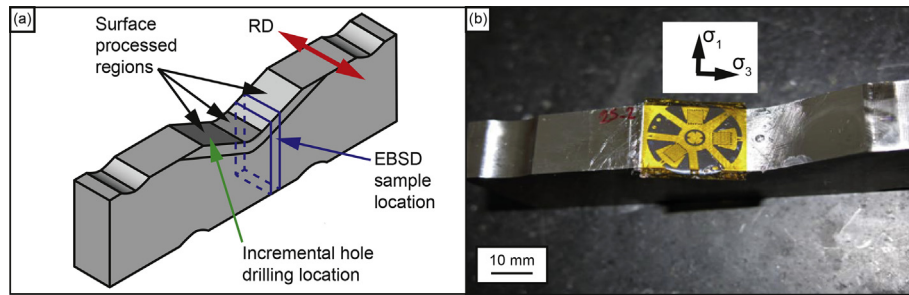
Fig. 1. (a) Schematic drawing of the surfaces processed with MSP and LSP, showing the material rolling direction (RD), EBSD sample section location and incremental hole drilling location. (b) Photograph of a 120° strain gauge rosette bonded to the processed surface of one of the samples for residual stress measurement by incremental hole drilling. The stress directions resolved by the technique are represented by σ_1 and σ_3.
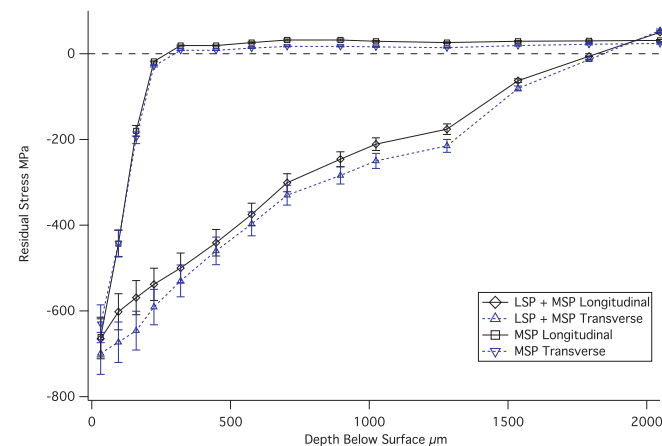
3. Results

3.1. Incremental hole drilling results

The residual stress profile as measured by incremental hole drilling in the location shown in Fig. 1(a), extends to a depth of approximately 250 μm for the MSP sample and approximately 1800 μm for the LSP + MSP sample. There is no marked difference between the residual stress measured in line with the rolling direction and transverse to the rolling direction. The results obtained from the incremental hole drilling of the MSP sample and the LSP + MSP sample are shown in Fig. 2. Incremental hole drilling was not performed on the LSP sample as the depth of residual stress would be the same as in the LSP + MSP sample.

3.2. EBSD results

Although some deformation twinning can clearly be observed in optical microscopy and scanning electron microscopy (SEM), EBSD is superior at being able to highlight the location of deformation twinning due to the crystallographic orientation contrast in the inverse pole figure maps, as is evident in Fig. 3. The deformation twinning in the MSP and the LSP + MSP samples is dominated by $\{10\bar{1}2\}$ deformation twinning of the α-phase grains. The $\{10\bar{1}2\}$ deformation twins are outlined in red in Fig. 3(b), (d) and (f). There is also a low volume fraction of $\{11\bar{2}1\}$ twins outlined in yellow. Two of the regions where $\{11\bar{2}1\}$ twins are present are shown in the higher magnification regions of Fig. 3(a), (b), (e) and (f). From the EBSD scans it is possible to measure the depth of deformation

twinning to be approximately 70 μm in the MSP and the LSP + MSP samples. The LSP sample exhibits no deformation twinning in the EBSD scans, see Fig. 3(c) and (d). All samples, including the LSP sample show shear bands observable in the EBSD scans. One of the regions where slip bands are visible is highlighted with a higher magnification region of Fig. 3(d) showing local misorientation.
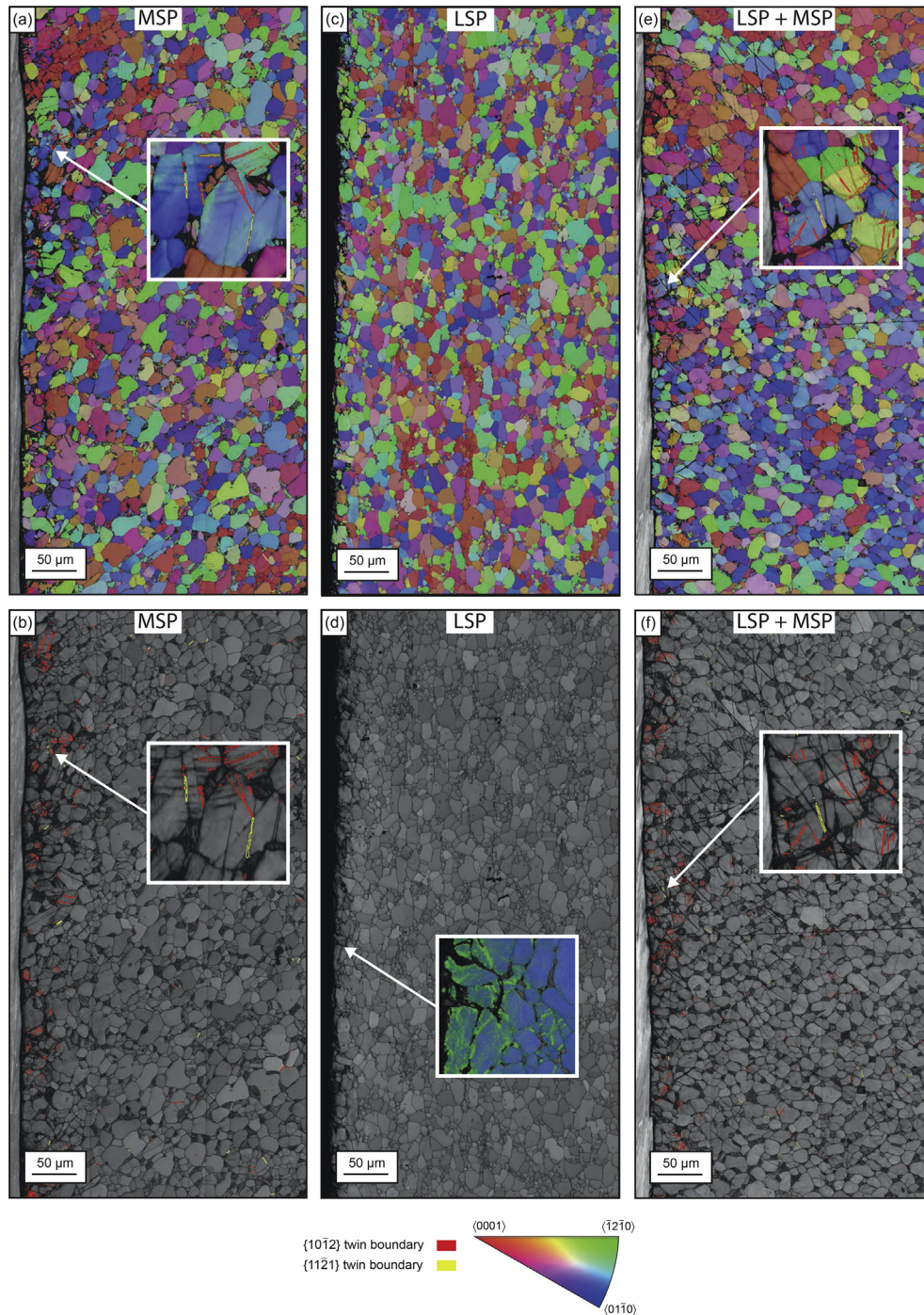
Using the EBSD data it is possible to estimate the depth of the residual stress by analysing the Grain Orientation Spread (GOS). The GOS maps were generated using a misorientation angle of 1° for α-phase grain boundaries to avoid incorrect GOS readings over macrozones [36] and individual low angle grain boundaries. The GOS results from the EBSD scans in Fig. 3 are shown in Fig. 4(a), (d) and (g). By eye it is possible to identify a line that correlates with a step change in the scans at a depth of approximately 100 μm for the MSP and LSP + MSP samples and approximately 50 μm for the LSP sample. However, a large amount of data is produced during EBSD map acquisition that can be analysed more effectively in graphical plots of all the data points. From analysing EBSD maps just by eye it is possible to miss subtle changes in intensity. Instead, plotting the GOS for each grain in the EBSD scan against distance from the surface is a more quantitative method for estimating the depth of the residual stress, as shown in Fig. 4(b), (e) and (h). In this way, the residual stress depth for the MSP sample can be estimated to be 200 μm by plotting the differential of a fourth order polynomial line fitted to the data points (Fig. 4(c)).

It is evident that the LSP and LSP + MSP data in Fig. 4(f) and (i) do not converge to a constant derivative of zero. Furthermore, Both the LSP and LSP + MSP data show a very similar trend. When considering the observation of the non-convergent derivatives in combination with the incremental hole drilling results in Fig. 2 it was apparent that larger area EBSD scans to deeper depths were required. An EBSD scan to a depth of 4.5 mm was conducted to evaluate the level of residual stress at deeper depths in the LSP + MSP sample using the GOS technique (Fig. 5). There is more noise in the large area scan so the trend is more subtle, but the point of inflection for the derivative as seen in Fig. 5(c), and therefore the estimated depth of the residual stress from the GOS analysis is 2 mm.

3.3. TEM results

TEM was used to investigate the dislocation structures present in each of the samples and to investigate if any microstructural features existed in the samples that were not resolvable by SEM. Results were obtained from all samples at the surface and 100 μm depth by electropolishing TEM specimens and FIB lamella extraction.

The MSP sample exhibited a high density of large deformation twins in the TEM foils taken from the surface (Fig. 6(a) and (b)).


Fig. 2. Incremental hole drilling results, graphically representing the sub-surface residual stress profile for MSP sample and LSP + MSP sample in the longitudinal and transverse to rolling directions.

Fig. 3. EBSD maps of the sectioned surface processed samples, inverse pole figure colouring and band contrast with {10$\bar{1}$2} twins highlighted with red twin boundaries and {11$\bar{2}$1} twins highlighted with yellow twin boundaries. (a) MSP, (c) LSP and (e) LSP + MSP samples: Inverse pole figure colouring with occurrences of {11$\bar{2}$1} highlighted in (e). (b) MSP, (d) LSP and (f) LSP + MSP samples: band contrast with shear banding highlighted in (d). (For interpretation of the references to colour in this figure legend, the reader is referred to the web version of this article.)

There was also a high dislocation density present, consistent with significant levels of plastic deformation during MSP. However, the material was so deformed that it was difficult to find a zone axis in the TEM that showed the dislocation structures clearly. Furthermore the samples from the surface were a challenge to analyse because of the craters that were created by the impact of the metallic shot with the surface. Some dislocation tangles that could be imaged from the surface are shown in Fig. 6(d) and (e). The TEM foils taken from the surface of the LSP sample did not contain any

large deformation twins and only two nanoscale deformation twins were observed right at the surface (Fig. 6(c)). The smaller of the two deformation twins present in the LSP sample was measured to be 30 nm and the larger one 70 nm wide. The dislocations in the LSP sample were easy to image separately with much more defined and planar dislocation structures as shown in Fig. 6(f).

At 100 μm deep below the processed surface the MSP sample no longer contained any deformation twin traces and the dislocations were noticeably easier to image than at the surface. There was a
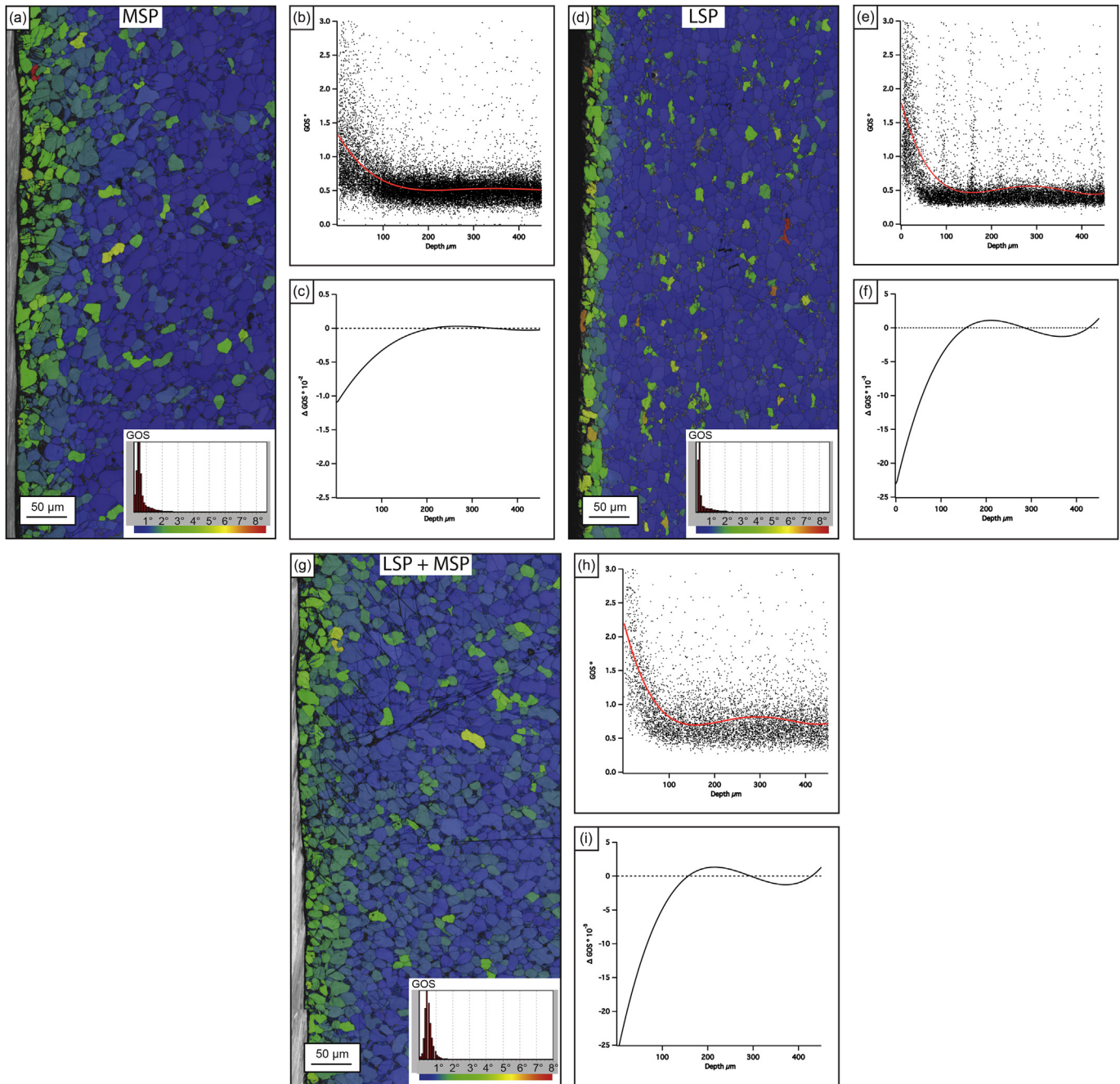
Fig. 4. (a) MSP, (d) LSP and (g) LSP + MSP samples: Grain Orientation Spread (GOS) maps. (b) MSP, (e) LSP and (h) LSP + MSP samples: GOS measurements plotted against depth from surface, curve fitted with a fourth order polynomial function. (c) MSP, (f) LSP and (i) LSP + MSP samples: differential of polynomial fitted curve to GOS data.

high dislocation density with large shear bands and dislocation structures with long wavy dislocation tangles, as is evident in Fig. 7(a)–(c). The LSP sample exhibited a reduced level of dislocation tangles, and the dislocation structures consisted of more directional arrays of planar dislocations, as is evident in Fig. 7(d)–(f). The dislocation structures exhibited a cellular structure in places, forming defined dislocation structures with planar edges. The LSP + MSP sample exhibited a combination of both effects. In Fig. 7(g) there is evidence of extensive dislocation tangles and cellular dislocation structures, as shown in Fig. 7(h) and (i).

Some of the dislocation networks in the LSP sample formed small sub-grains with low angle grain boundaries. TEM micrographs of some of the sub-grains and TKD analysis of the low angle

boundaries are shown in Fig. 8. TKD was performed to analyse the misorientations between the sub-grains because applying the selected area aperture on the sub-grain boundaries in the TEM yielded a single crystal diffraction pattern. TKD enables TEM specimens to be scanned with EBSD. In TKD mode the spatial resolution is much greater than conventional EBSD as the interaction volume is greatly reduced when the electrons are transmitted through the specimen [37,38]. The smallest sub-grains at the centre of the TKD scan in Fig. 8(b) had no measurable misorientation beyond the normal orientation spread within the parent grain. The slightly larger sub-grains to the right of the scan did have a measurable misorientation of 5° to 6° misorientation from the parent grain.
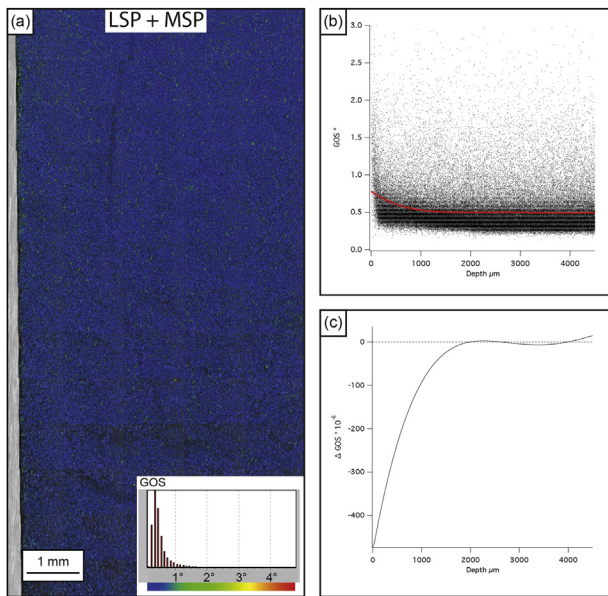
Fig. 5. (a) LSP + MSP sample GOS map to a depth of 4.5 mm (b) GOS measurements plotted against depth from surface, curve fitted with a fourth order polynomial function. (c) differential of polynomial fitted curve to GOS data.

4. Discussion

The human brain and eyes are excellent at noticing patterns and anomalies in images. However, without plotting the GOS measurements against the measurement depth it is difficult to determine the depth where the GOS reduces to the minimum value. Instead the eye is drawn to the more pronounced contrast in the grains that have a high GOS value and hence bright colouring. The MSP sample residual stress depth from incremental hole drilling was measured to be approximately 250 μm, while the GOS measurements estimated it to be approximately 200 μm. For the LSP + MSP sample the incremental hole drilling measured the residual stress depth to be approximately 1800 μm and the GOS measurements estimated it to be 2000 μm. Unfortunately it is not possible to use incremental hole drilling and EBSD in exactly the same area so there will be some variation in the exact depth of the residual stress due to local variations in the material. However, the results demonstrate that GOS measurements correctly estimate the depth of residual stress in Ti—6Al—4V which contrasts with the findings by Child et al. in nickel-based superalloys [21]. To estimate correctly the depth it is necessary to use a large area that covers the entire depth of the residual stress. Unfortunately, the acquisition time for such large EBSD maps is still too long for most practical applications. The maps presented in this paper took 12—24 h to acquire. Furthermore, careful interpretation of the plotted data in Fig. 4 is necessary. The derivative of the fourth order polynomial fit of the MSP data (Fig. 4(c)) converges to an acceptable level beyond 200 μm depth. However, the derivatives of the fourth order polynomials fitted to the LSP data set and the LSP + MSP data set do not converge to satisfactory levels (Fig. 4(f) and (i)). The derivative of the fourth order polynomial fitted to the deeper scan of the LSP + MSP sample in Fig. 5(c) does converge to an acceptable level beyond 2 mm depth, ten times the depth of Fig. 4(f) and (i). The residual stress depth of the samples would have been interpreted incorrectly if the data for the LSP and the LSP + MSP samples in Fig. 4(f) and (i) had been fitted with a function that forces convergence.
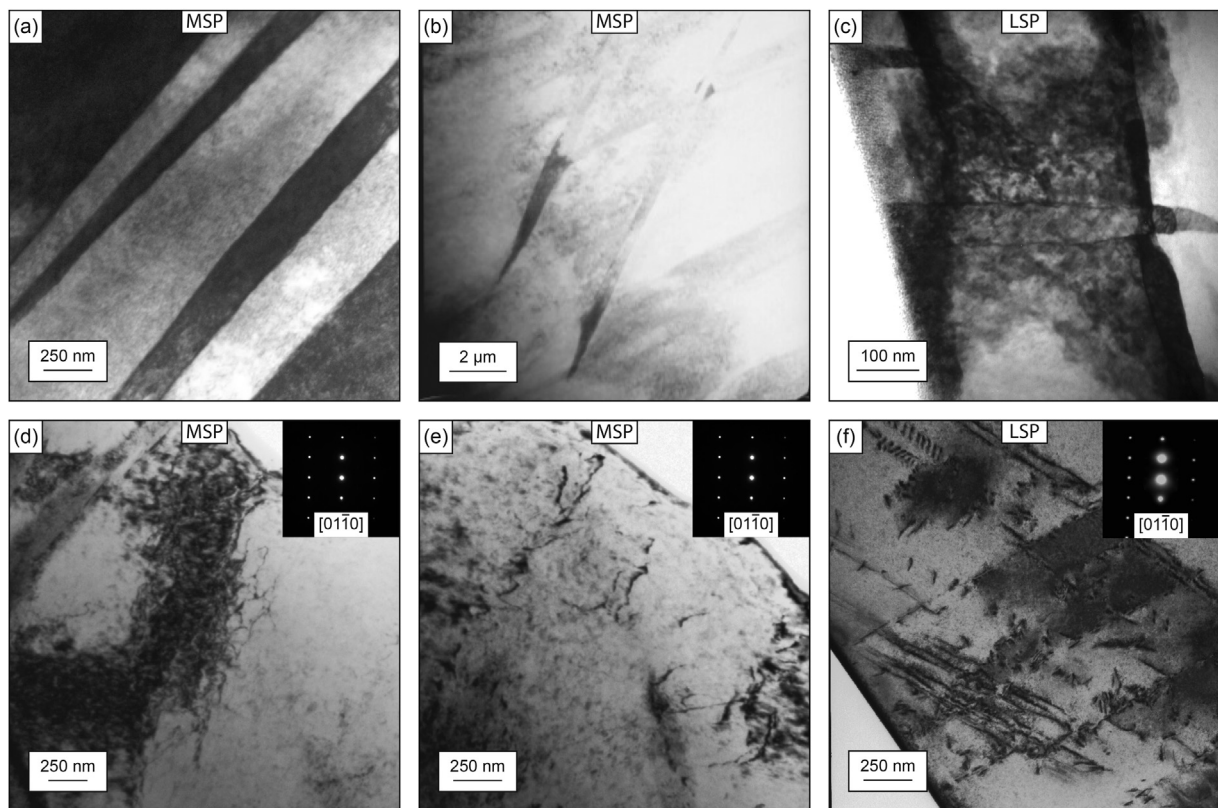
Fig. 6. Bright field TEM micrographs from the surface grains. (a) and (b) Deformation twins in the MSP sample. (c) Nanoscale deformation twins in the LSP sample. (d) and (e) Dislocation structures in the MSP sample with corresponding selected area diffraction patterns. (f) Dislocation structures in the LSP sample with corresponding selected area diffraction patterns.
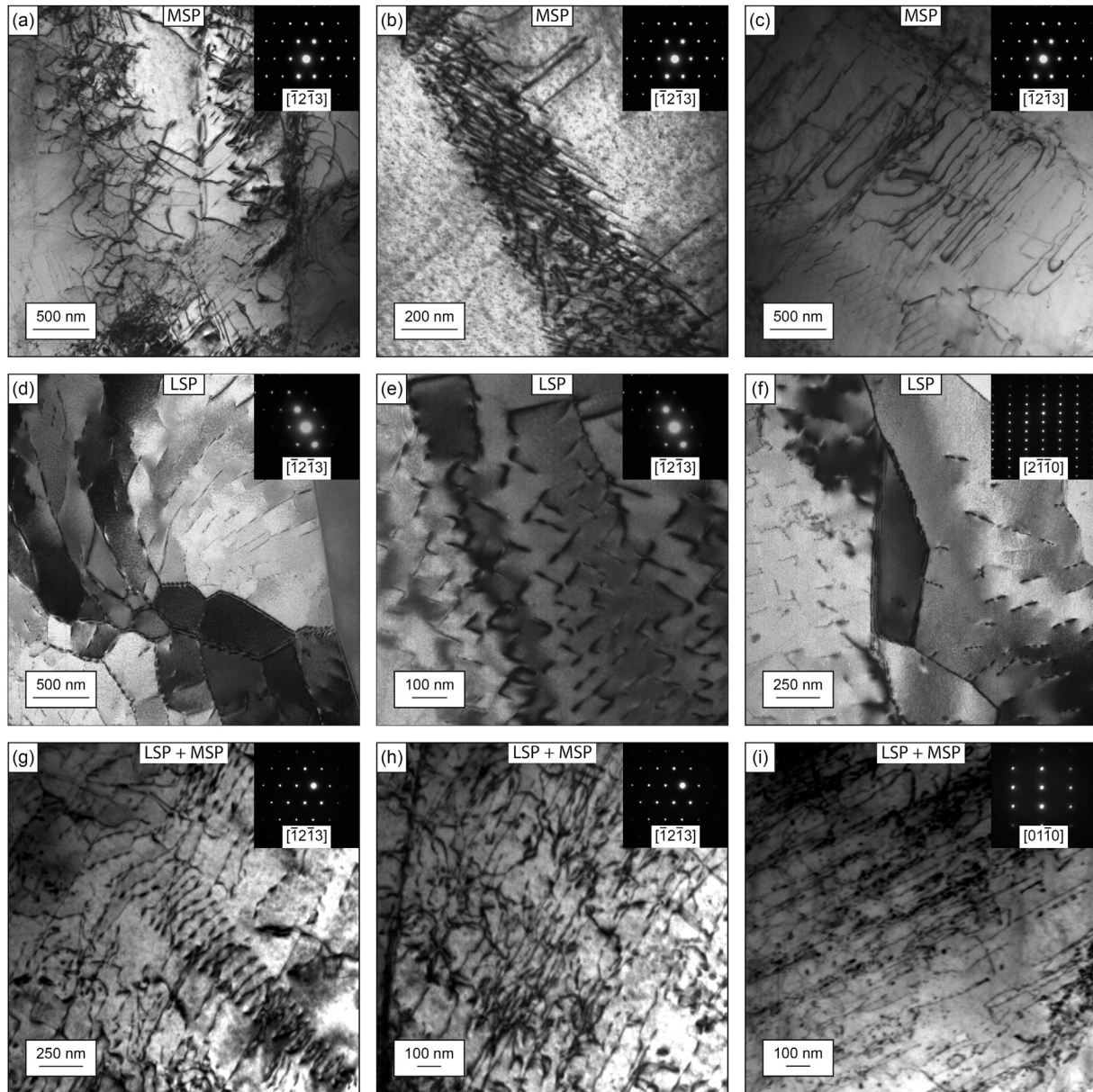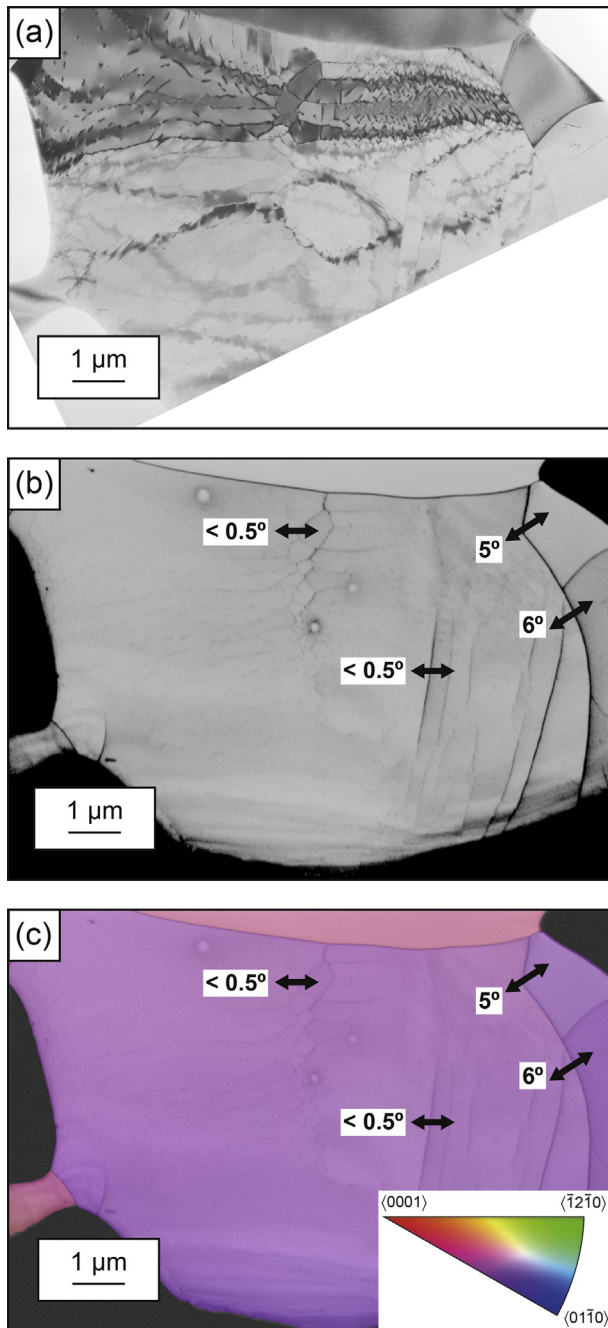
Fig. 7. Bright field TEM micrographs from 100 μm below the processed surfaces with corresponding selected area diffraction patterns. (a) to (c) Dislocation structures in the MSP sample. (d) to (f) Dislocation structures in the LSP sample. (g) to (i) Dislocation structures in the LSP + MSP sample.

Further analysis was conducted on the GOS data to ensure that the results were due to the residual stress, and were not an artefact of the decaying polynomial function that was used to fit the data. For the MSP sample the first 50 μm and 100 μm depth of data were removed from the data set (Fig. 9). The same check was conducted on the LSP + MSP sample, with the first 100 μm and 200 μm depth removed (Fig. 10). In both cases a decreasing trend was still present in the data. In Figs. 9 and 10 a decaying exponential fit function was used to ensure that the differential converged to zero. By contrast a polynomial function was used in Figs. 4 and 5 to determine if the data had converged to a constant value.

The 4.5 mm deep LSP + MSP scan contains a substantial amount of noise, which means that the fitted curve exhibits a weak trend. One standard deviation above the mean of the settled data is 0.62° which would intersect the line of best fit at approximately 400 μm depth. However the data indicates a change at approximately 2 mm. The trend is most easily observed by analysing the minimum

GOS values in Fig. 10(a) where the GOS measurements settle to approximately 0.2° at the 2 mm depth. At depths shallower than 2 mm below the surface the minimum values for the GOS are slightly increased. The effect size is small and the sample size is sufficiently large (over 150,000 grains) that the effect is statistically relevant.

The 70 μm depth of deformation twinning that was measured by EBSD in both the MSP and LSP + MSP samples is due to the MSP process alone. This is confirmed by the EBSD results from the LSP sample where there was no deformation twinning of a size large enough to be indexed by EBSD. Furthermore, TEM analysis of the LSP sample did not produce evidence for a high density of fine deformation twins. There were just two cases of nanoscale deformation twins in the FIB samples taken from close to the surface. This observation contrasts with conventional wisdom that increased strain rates favour deformation twinning over dislocation motion [39]. To rationalise the absence of deformation twinning in

Fig. 8. (a) Lower magnification bright field TEM micrograph of sub-grains in the LSP sample shown in Fig. 7(d). (b) TKD EBSD band contrast image of the same region in (a). (c) TKD EBSD inverse pole figure colour image of low angle sub-grain boundaries. (For interpretation of the references to colour in this figure legend, the reader is referred to the web version of this article.)

of the material, there is insufficient time for the heat to be conducted deeper into the material. Furthermore, the transfer from kinetic energy to thermal energy by elastic deformation during the propagation of the elastic shock wave does not preclude deformation twinning in other high strain rate deformation processes. Therefore, the presence of deformation twinning during other high strain rate processes suggests that any local increase in temperature cannot explain the absence of deformation twinning from the LSP sample. Compressive loading also increases the likelihood of deformation twinning relative to loading in tension [46]. On a microscopic scale there is reported to be a strong link between grain size and deformation twinning: larger grains are more prone to deformation by twinning than small grains [39,47,48]. The grain size in the Ti−6Al−4V LSP sample is small (≈ 10 μm), but it was noticeable that the MSP sample with the same grain size did deform by deformation twinning.
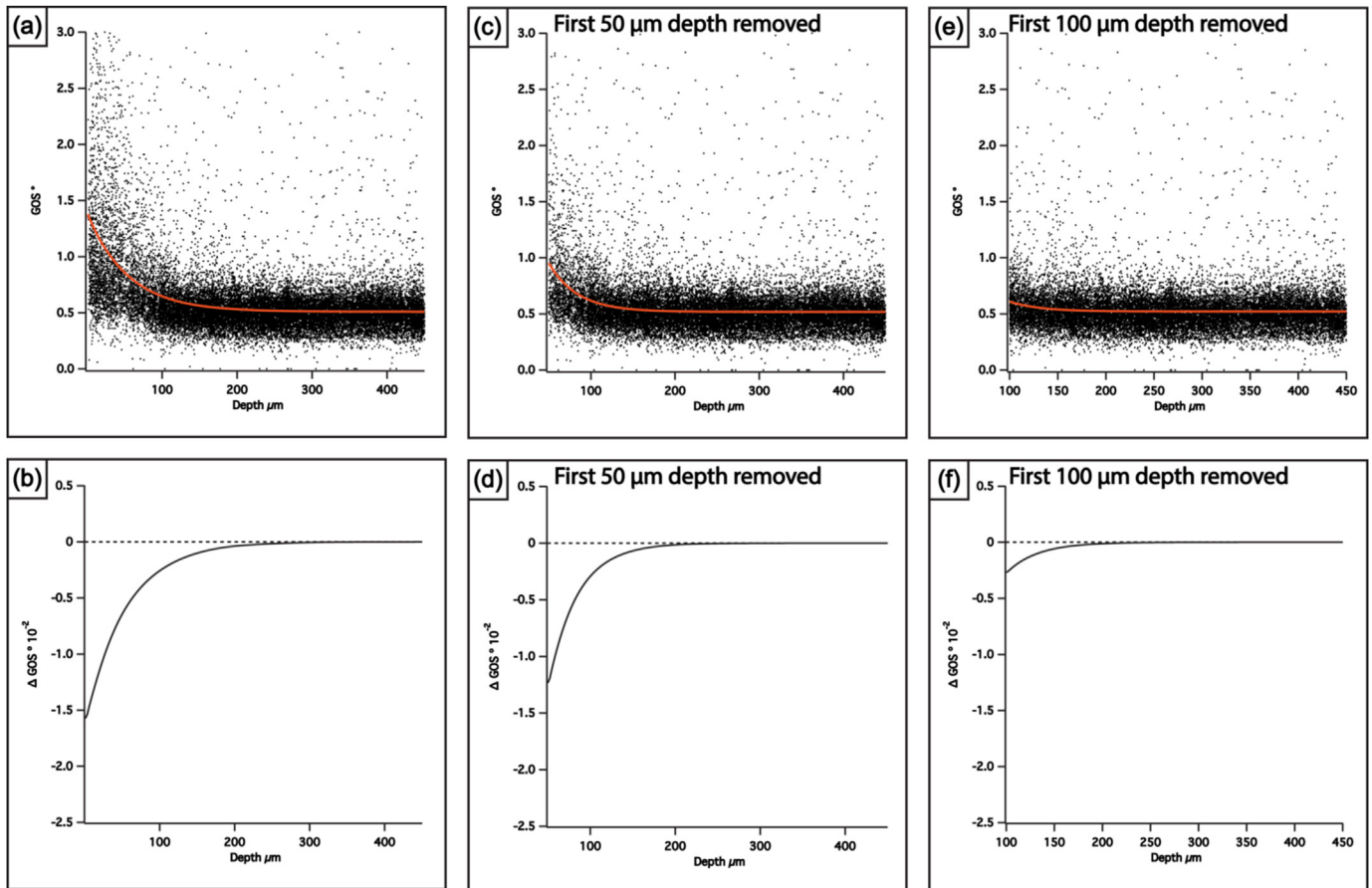
The most significant difference between MSP and LSP is the type of loading. The strain rate from LSP is higher because the deformation is due to the explosive shock wave of the ablative layer and the extent of strain during LSP is lower than for MSP [49]. The strain rate for MSP is dependent on the processing parameters: fine shot media size (0.15 mm) and high shot velocity (100 m s^{-1}) produces the highest strain rate deformation [50]. The average MSP strain rate has been estimated to be approximately 10^4 s^{-1} with peak localised strain rates of approximately 10^5 s^{-1} [50−53]. In ballistic testing of Ti−6Al−4V we have observed that at very high strain rates $\{10\bar{1}2\}$ deformation twinning actually becomes less prevalent. These observations are consistent with those by Gray III [54,55].

During these very high strain rate conditions, $\{11\bar{2}1\}$ deformation twinning occurs more frequently than $\{10\bar{1}2\}$ twinning. The change from $\{10\bar{1}2\}$ twinning to $\{11\bar{2}1\}$ twinning can be rationalised by $\{10\bar{1}2\}$ having a more complex shuffle mechanism compared to $\{11\bar{2}1\}$ twinning [56]. Therefore, it is reasonable to assume that $\{10\bar{1}2\}$ twinning cannot form as rapidly as $\{11\bar{2}1\}$ twinning during very high strain rate deformation. $\{11\bar{2}1\}$ twinning has the simplest shuffle complexity of the deformation twin types in titanium. It is also plausible that there may also be an upper limit on the strain rate that can be accommodated by $\{11\bar{2}1\}$ twinning before another mechanism becomes favourable. From the LSP results there is potential evidence of a dislocation mechanism that is capable of higher rate strain accommodation than $\{11\bar{2}1\}$ twinning. Hence, the lack of deformation twinning can be rationalised as a consequence of an upper limit to the rate of strain for deformation twinning in Ti−6Al−4V. The approximate strain rates for MSP and LSP are shown in Fig. 11 with the corresponding microstructures that have been observed at low, high and very high strain rates. The loading condition strain rates are as described by Field et al. [57].

The theories that govern the production of dislocations by Frank-Read sources and conventional dislocation mechanics are commonly considered to only allow the movement of dislocations to occur at a maximum velocity of the transverse speed of sound in the material [58−62]. However, such extensive dislocation networks in the LSP sample adds evidence to the theory that during very high strain rate deformation processes, dislocations are capable of forming almost instantaneously, as predicted by Hirth and Lothe [63]. It is not possible from the results presented in this work to confirm the theory of 'homogeneous nucleation' as proposed by Gurrutxaga-Lerma et al. [64] and Shehadeh et al. [65] for cubic materials. Nevertheless, it is evident that to understand the observations reported here for LSP processed material that further research is required on dislocation dynamics at high strain rates.

It was apparent from the TEM foils (Fig. 6(d) and (e)) at the surface of the MSP sample that extensive deformation had taken place with many dislocations and deformation twins present, consistent with the deformed structures expected from high strain

the LSP sample it is necessary to examine the conditions under which deformation twinning is known to operate in Ti−6Al−4V.

There is abundant evidence of deformation twinning occurring in Ti−6Al−4V that has been subjected to high strain rate deformation or cryogenic temperature deformation [40−45]. Here, we know that LSP is subjecting the material to a very high strain rate ($>10^6$ s^{-1}) which conventional wisdom would assume that deformation twinning would therefore be increasingly favoured relative to deformation by slip. LSP is conducted at room temperature, and although some local heating from the LSP will occur at the surface

Fig. 9. (a) MSP GOS data from Fig. 4(a) fitted with a decaying exponential function. (b) Differential of fitted data in (a) showing residual stress depth of approximately 200 μm. (c) MSP GOS data from (a) with the first 50 μm depth of data removed. (d) Differential of fitted data in (c). (e) MSP GOS data from (a) with the first 100 μm depth of data removed. (f) Differential of fitted data in (e).

rate deformation. However, the dislocation density observed was lower than that which was observed by Messé et al. in MSP processed nickel-based superalloy, Udimet© alloy 720 Li [66]. This observation is consistent with the fact that there are fewer slip systems in Ti—6Al—4V than in nickel-based superalloys, and so deformation twinning in Ti—6Al—4V is vitally important for plastic deformation. It is therefore surprising that the LSP sample facilitates plastic deformation without deformation twinning. As shown in Figs. 6 and 7, the change from tangled wavy slip in the MSP sample to planar slip in the LSP sample is consistent with observations by Sevillano et al. [67]. The change is due to the increased strain rate [55]. Dislocation tangles suggest that slip has taken place on multiple slip systems, while more planar slip suggests that fewer slip systems have been activated. The formation of dislocation cells in the LSP sample suggests that work hardening has taken place.

The mechanism of MSP causes multidirectional deformation, and individual shots can impact the surface where another shot has already landed. The process of multiple impacts in slightly different directions causes multiple slip systems to be activated and causes work hardening through dislocation interactions. In contrast to this, the mechanism of LSP is more planar with shock waves that are always generated normal to the surface with less overlap. Fewer slip systems are activated which leads to more planar dislocation structures.

The results from the 100 μm depth LSP sample in Fig. 7 are consistent with observations by Trdan et al. in aluminium alloy EN AW 6082-T651 and by Lu et al. in aluminium alloy LY2 [18,19]. Dislocation cells cause the material to sub-divide into microscale

and nanoscale grains. The refined microstructure in the LSP treated zone will benefit from some increased strength due to Hall—Petch strengthening from the refined grain size. The micrographs reported by Trdan et al. have a striking resemblance to Fig. 7. As described by Trdan et al. and Lu et al. [19], grain refinement is an effective way to provide dislocation annihilation and energy minimisation so it would be energetically favourable for the complex arrays of dislocations to form sub-grains. However the TKD results observed in Fig. 8 show that the misorientation between the majority of the sub-grains that were observed is extremely low, so they are only actually cellular dislocation structures. Once the small sub-grains or cellular dislocation structures have been formed by LSP an amount of strain could potentially be taken up by grain rotation. Grain rotation following sub-grain generation would explain the higher misorientations of 5° and 6° observed in Fig. 8.

The cellular dislocation structures are similar to those observed from hot working of Ti—6Al—4V. TEM foils were analysed from an undeformed region of the sample to observe the background dislocation structures remaining from the hot working processes. Two occurrences of spherical dislocation loops and a low dislocation density of wavy dislocation tangles were observed. No planar dislocation structures or sub-grains were present in the undeformed material. Therefore, some of the dislocation tangles observed in the specimens are due to the background dislocation density rather than to the MSP and LSP processing.

It is likely that the planar dislocation structures are associated to the reduction in deformation twinning at very high strain rates. Other researchers have shown a relationship between small grain
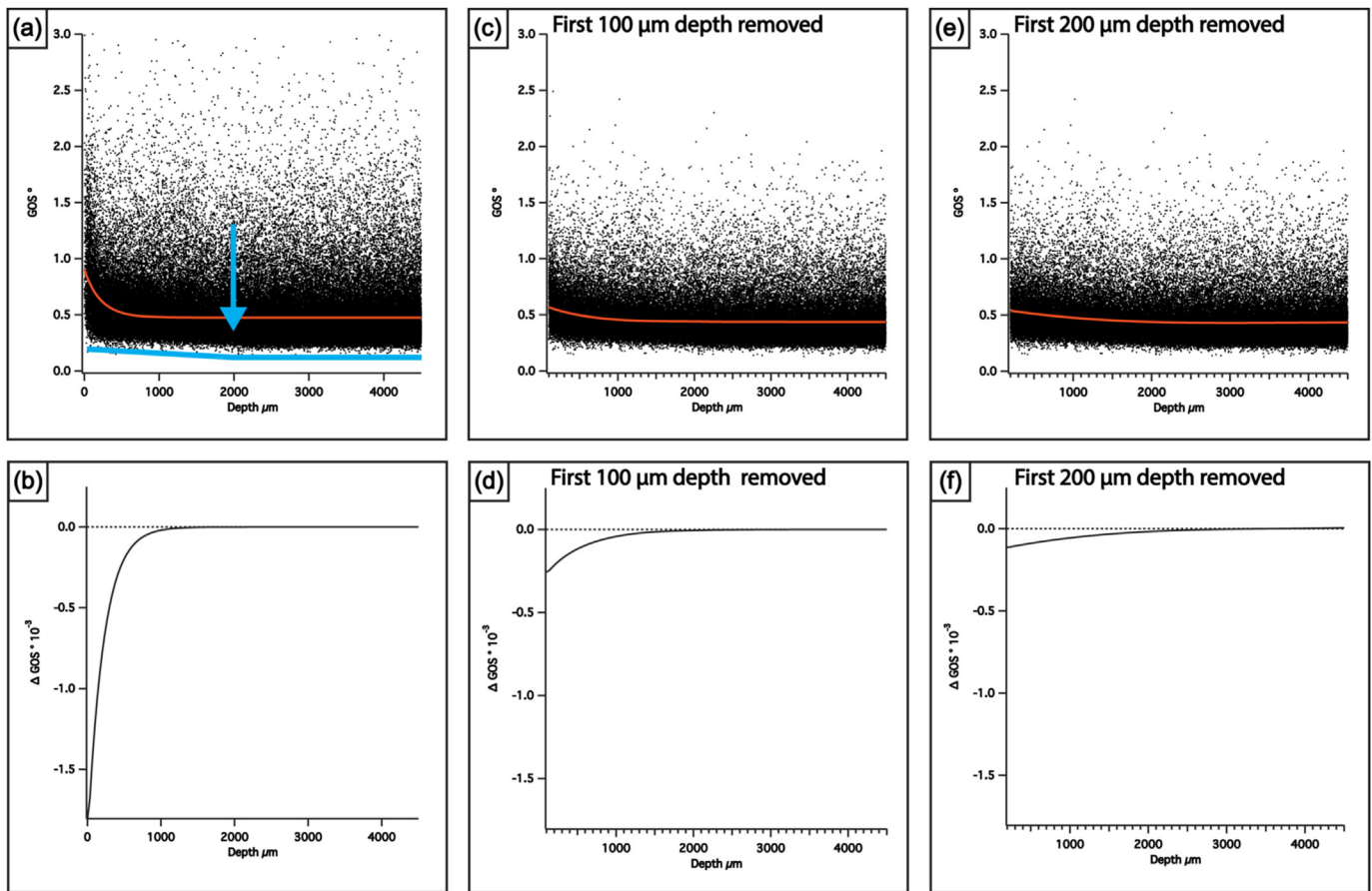
Fig. 10. (a) LSP + MSP GOS data from Fig. 5(a) fitted with a decaying exponential function. The blue line and the blue arrow shows qualitative analysis of the GOS data with a step change at 2000 μm depth. (b) Differential of fitted data in (a). (c) LSP + MSP GOS data from (a) with the first 100 μm depth of data removed. (d) Differential of fitted data in (c). (e) LSP + MSP GOS data from (a) with the first 200 μm depth of data removed. (f) Differential of fitted data in (e). (For interpretation of the references to colour in this figure legend, the reader is referred to the web version of this article.)

size and a reduced propensity for titanium alloys to deform by deformation twinning [68,69]. However, the reduction in the expected amount of deformation twinning during LSP cannot be explained by the grain refinement as the dislocation structures and subsequent sub-grains cannot be generated in the femtoseconds of time before any very limited deformation twinning can take place in the timescale of the LSP event causing plastic deformation. It is likely that that the strain rate during LSP is too high and the time scale over which a given region experiences strain is too short to allow the formation of deformation twins. There is insufficient time for the repositioning of the atoms to a twinned orientation to accommodate the deformation. It is unlikely that the extent of strain during LSP would be low enough to preclude nanoscale deformation twinning but high enough to induce deep compressive residual stress profiles.

5. Conclusions

GOS measurements from EBSD scans have been shown to correlate with the residual stress depth measured by incremental hole drilling in Ti−6Al−4V for MSP and LSP. However, it is important to recognise that others, such as Child et al. made contrasting findings of half of the depth predicted by GOS analysis in nickel-based superalloys [21]. The finding does however mean that EBSD can compliment incremental hole drilling when the long acquisition time for the EBSD scans and sectioning of the material for metallographic preparation are feasible.

MSP induced deformation twinning to a depth of 70 μm. However, by contrast, LSP induced limited nanoscale deformation twinning in the surface grains (the first 10 μm), and deformation twinning was absent at deeper depths. The lack of deformation twinning in the LSP sample was an unexpected finding of this study. The deformation mechanisms of Ti−6Al−4V under very high ($>10^6$ s^{-1}) strain rate during LSP have been shown to be different to what is expected of Ti−6Al−4V under conventional high strain rate deformation. We postulate that high-speed dislocations may have accommodated the very high strain rate deformation during LSP. The finding provides further evidence for theories of high-speed dislocations proposed by other researchers [63−65]. However, further research is required to understand very high strain rate deformation.

MSP produces long wavy tangled dislocation structures and shear bands. LSP produces more directional planar dislocations and networks of dislocation cells and sub-grains. Although, in most of the cases observed, what appears to be sub-grains based on bright field image contrast in the TEM did not exhibit a high enough degree of misorientation in TKD to be considered grain boundaries. The morphology of the dislocation structures observed here were very similar to those presented by Trdan et al. and by Lu et al. in aluminium alloys [18,19]. However we suggest that caution should be exercised in describing dislocation cells as sub-grains unless the misorientation has been characterised. The observation of more planar dislocation structures in LSP is rationalised by the higher strain rate and the more planar nature of the shock wave compared
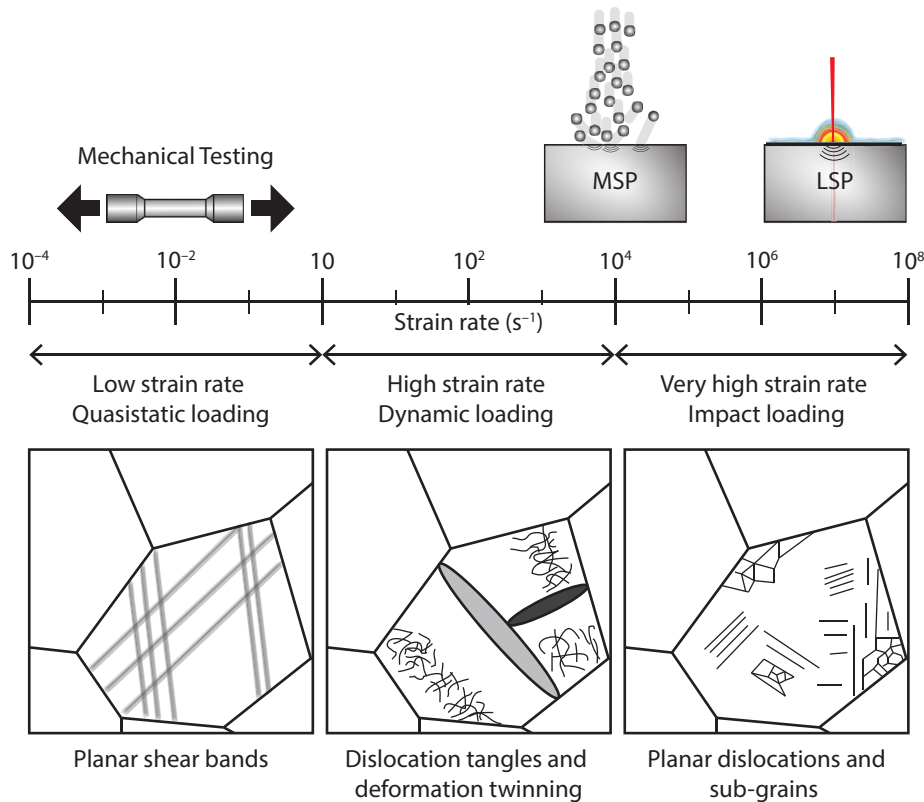
Fig. 11. Approximate strain rates for mechanical testing, MSP and LSP with corresponding drawings of deformation structures in Ti—6Al—4V. Low strain rate quasistatic loading produces planar shear bands, high strain rate deformation such as MSP produces dislocation tangles and deformation twinning and very high strain rate deformation such as LSP produces planar dislocation structures and sub-grains with little or no deformation twinning.

to the multidirectional nature of the multiple impacts from MSP. Furthermore, the individual shock loading points of LSP do not overlap in the way that they do during MSP. The tangled dislocation structures produced by MSP are due to the localised work hardening from multiple subsequent shot impacts.

A combination of the two techniques (LSP followed by MSP) produces a beneficial deep compressive residual stress and a work hardened surface layer beyond that possible with either technique alone.

References

[1] SAE Standard 2430, Shot Peening AMS Standard, SAE International, Pennsylvania, 1948.
[2] W.J. Harris, Report on: the Influence of Fretting on Fatigue. Part III, 1972. Paris.
[3] P.E. Cary, History of shot peening, in: Int. Conf. Shot Peen, ICPS-1, Paris, 1981.
[4] E.G. Herbert, The work hardening of steel by abrasion, with an appendix on the "cloudburst" test and super hardening, J. Iron Steel 11 (1927) 265.
[5] E.G. Herbert, The Herbert cloudburst hardness testing machine, Eng. July (1928) 28.
[6] J.O. Almen, Shot blasting test, US patent No. 2350440, 1944.
[7] R.L. Mattson, J.O. Almen, Final Report on: Effect of Shot Blasting on Physical Properties of Steel, 1944.
[8] J.O. Almen, Application of shot peening, Plast. Work. Met. 1 (1964) 20.
[9] E. Hawkinson, Shot peening — history, in: SAE ISTC Div. 20 Mech, Prestress, Metyals, Colorado, 1962.
[10] G.F. Bush, J.O. Almen, L.A. Danse, J.P. Heiss, How, when and by whom was mechanical prestressing discovered, in: Bienn. Meet. Div. 20, SAE, ISTC, 1962.
[11] J. Champaigne, History of shot peening specifications, Shot Peen. Mag. 20 (2006) 12.
[12] C.S. Montross, T. Wei, L. Ye, G. Clark, Y.-W. Mai, Laser shock processing and its effects on microstructure and properties of metal alloys: a review, Int. J. Fatigue 24 (2002) 1021.
[13] X.C. Zhang, Y.K. Zhang, J.Z. Lu, F.Z. Xuan, Z.D. Wang, S.T. Tu, Improvement of fatigue life of Ti—6Al—4V alloy by laser shock peening, Mater. Sci. Eng. A 527 (2010) 3411.
[14] R. Fabbro, P. Peyre, L. Berthe, X. Scherpereel, Physics and applications of laser-shock processing, J. Laser Appl. 10 (1998) 265.
[15] I. Altenberger, R.K. Nalla, Y. Sano, L. Wagner, R.O. Ritchie, On the effect of deep-rolling and laser-peening on the stress-controlled low- and high-cycle fatigue behavior of Ti—6Al—4V at elevated temperatures up to 550 °C, Int. J. Fatigue 44 (2012) 292.
[16] A.K. Gujba, M. Medraj, Laser peening process and its impact on materials properties in comparison with shot peening and ultrasonic impact peening, Materials 7 (2014) 7925.
[17] Y.W. Fang, Y.H. Li, W.F. He, P.Y. Li, Effects of laser shock processing with different parameters and ways on residual stresses fields of a TC4 alloy blade, Mater. Sci. Eng. A 559 (2013) 683.
[18] U. Trdan, M. Skarba, J. Grum, Laser shock peening effect on the dislocation transitions and grain refinement of Al-Mg-Si alloy, Mater. Charact. 97 (2014) 57.
[19] J.Z. Lu, K.Y. Luo, Y.K. Zhang, C.Y. Cui, G.F. Sun, J.Z. Zhou, L. Zhang, J. You, K.M. Chen, J.W. Zhong, Grain refinement of LY2 aluminum alloy induced by ultra-high plastic strain during multiple laser shock processing impacts, Acta Mater 58 (2010) 3984.
[20] S.J. Lainé, K.M. Knowles, {11$\bar{2}$4} deformation twinning in commercial purity titanium at room temperature, Philos. Mag. 95 (2015) 2153.
[21] D.J. Child, G.D. West, R.C. Thomson, Assessment of surface hardening effects from shot peening on a Ni-based alloy using electron backscatter diffraction techniques, Acta Mater 59 (2011) 4825.
[22] S.I. Wright, M.M. Nowell, D.P. Field, A review of strain analysis using electron backscatter diffraction, Microsc. Microanal. 17 (2011) 316.
[23] ASTM Standard E837—13a, Standard Test Method for Determining Residual Stresses by the Hole-drilling Strain-gage Method, ASTM International, West

Conshocken, 2013.

[24] E. Macherauch, P. Müller, Das $\sin^2\psi$-Verfahren der röntgenographischen Spannungsmessung, Z. für Angew. Phys. 13 (1961) 305.

[25] ASTM Standard E2860—12, Standard Test Method for Residual Stress Measurement by X-Ray Diffraction for Bearing Steels, ASTM International, West Conshocken, 2014.

[26] J. Lu, A. Niku-Lari, J.-F. Flavenot, Récents développements de la mesure des contraintes résiduelles par perçage incrémental, Matériaux Tech. 73 (1985) 709.

[27] B.R. Sridhar, W.G. Nafde, K.A. Padmanabhan, Effect of shot peening on the residual stress distribution in two commercial titanium alloys, J. Mater. Sci. 27 (1992) 5783.

[28] J. Lu, Prestress engineering of structural material: a global design approach to the residual stress problem, in: G.E. Totten, M. Howes, T. Inoue (Eds.), Handb. Residual Stress Deform. Steel, ASM International, Ohio, 2002.

[29] D. Walker, Residual stress measurement techniques, Adv. Mater. Process 159 (8) (2001) 30.

[30] M.E. Fitzpatrick, A.T. Fry, P. Holdway, F.A. Kandil, J. Shackleton, L. Suominen, Measurement Good Practice Guide No. 52, Determination of Residual Stresses by X-ray Diffraction, second ed., National Physical Laboratory, Middlesex, 2005.

[31] SAE Standard J442_201302, Test Strip, Holder, and Gage for Shot Peening, SAE International, Pennsylvania, 2013.

[32] SAE Standard AMS-2431/1, Peening Media (ASR), Cast Steel Shot, Regular Hardness (45 to 52 HRC), SAE International, Pennsylvania, 2011.

[33] W.L. Finlay, J. Resketo, M.B. Vordahl, Optical metallography of titanium, Ind. Eng. Chem. 42 (1950) 218.

[34] M.J. Donachie, Titanium: a Technical Guide, second ed., ASM International, Ohio, 2000.

[35] G. Lütjering, J.C. Williams, Titanium Engineering Materials and Processes, second ed., Springer, Berlin Heidelberg, 2007.

[36] D. Rugg, M. Dixon, F.P.E. Dunne, Effective structural unit size in titanium alloys, J. Strain Anal. Eng. Des. 42 (2007) 269.

[37] R.R. Keller, R.H. Geiss, Transmission EBSD from 10 nm domains in a scanning electron microscope, J. Microsc. 245 (2011) 245.

[38] P.W. Trimby, Orientation mapping of nanostructured materials using Transmission Kikuchi Diffraction in the scanning electron microscope, Ultramicroscopy 120 (2012) 16.

[39] J.W. Christian, S. Mahajan, Deformation twinning, Prog. Mater. Sci. 39 (1995) 1.

[40] R.E. Reed-Hill, in: R.E. Reed-Hill, J.P. Hirth, H.C. Rogers (Eds.), Role of Deformation Twinning in the Plastic Deformation of a Polycrystalline Anisotropic Metal, Deformation Twinning, New York, NY, 1964.

[41] P.S. Follansbee, G.T. Gray, An analysis of the low temperature, low and high strain-rate deformation of Ti-6Al-4V, Metall. Trans. A 20 (1989) 863.

[42] F. Coghe, W. Tirry, L. Rabet, D. Schryvers, P. Van Houtte, Importance of twinning in static and dynamic compression of a Ti—6Al—4V titanium alloy with an equiaxed microstructure, Mater. Sci. Eng. A 537 (2012) 1.

[43] J.L.W. Warwick, J. Coakley, S.L. Raghunathan, R.J. Talling, D. Dye, Effect of texture on load partitioning in Ti-6Al-4V, Acta Mater 60 (2012) 4117.

[44] E. Wielewski, C.R. Siviour, N. Petrinic, On the correlation between macrozones and twinning in Ti—6Al—4V at very high strain rates, Scr. Mater 67 (2012) 229.

[45] Z.W. Wyatt, W.J. Joost, D. Zhu, S. Ankem, Deformation mechanisms and kinetics of time-dependent twinning in an α-titanium alloy, Int. J. Plast. 39 (2012) 119.

[46] S. Mahajan, D.F. Williams, Deformation twinning in metals and alloys, Int. Metall. Rev. 18 (1973) 43.

[47] Q. Yu, Z.-W. Shan, J. Li, X. Huang, L. Xiao, J. Sun, E. Ma, Strong crystal size effect on deformation twinning, Nature 463 (2010) 335.

[48] H. Abdolvand, M.R. Daymond, Multi-scale modeling and experimental study of twin inception and propagation in hexagonal close-packed materials using a crystal plasticity finite element approach; part II: local behavior, J. Mech. Phys. Solids 61 (2013) 803.

[49] A.K. Gujba, M. Medraj, Laser peening process and its impact on materials properties in comparison with shot peening and ultrasonic impact peening, Materials 7 (2014) 7925.

[50] B. Alfredsson, E. Nordin, An elastic—plastic model for single shot-peening impacts, Tribol. Lett. 52 (2013) 231.

[51] K. Schiffner, C.D. gen. Helling, Simulation of residual stresses by shot peening, Comput. Struct. 72 (1999) 329.

[52] S.A. Meguid, G. Shagal, J.C. Stranart, 3D FE analysis of peening of strain-rate sensitive materials using multiple impingement model, Int. J. Impact Eng. 27 (2002) 119.

[53] S.M. Hassani-Gangaraj, A. Moridi, M. Guagliano, From conventional to severe shot peening to generate nanostructured surface layer: a numerical study, IOP Conf. Ser. Mater. Sci. Eng. 63 (2014) 012038.

[54] G.T. Gray III, Deformation twinning: influence of strain rate, in: TMS Meet. Symp. Twinning Adv. Mater., 1993. Pittsburgh.

[55] G.T. Gray III, High-strain-rate deformation: mechanical behavior and deformation substructures induced, Annu. Rev. Mater. Res. 42 (2012) 285.

[56] M.H. Yoo, Slip, twinning, and fracture in hexagonal close-packed metals, Metall. Trans. A 12A (1981) p.409.

[57] J.E. Field, S.M. Walley, W.G. Proud, H.T. Goldrein, C.R. Siviour, Review of experimental techniques for high rate deformation and shock studies, Int. J. Impact Eng. 30 (2004) 725.

[58] J. Weertman, High speed dislocations, in: P.G. Shewmon, V.F. Zackay (Eds.), Response of Metals to High Velocity Deformation, Interscience, New York, 1961.

[59] J. Weertman, Uniformly moving transonic and supersonic dislocations, J. Appl. Phys. 38 (1967) 5293.

[60] W.D. Nix, R.A. Menezes, Physics of strengthening mechanisms in crystalline solids, Annu. Rev. Mater. Sci. 48 (1971) 313.

[61] A. Roos, J.T.M. De Hosson, E. Van der Giessen, High-speed dislocations in high strain-rate deformations, Comput. Mater. Sci. 20 (2001) 19.

[62] B. Gurrutxaga-Lerma, The role of the mobility law of dislocations in the plastic response of shock loaded pure metals, Model. Simul. Mater. Sci. Eng. 24 (2016) 065006.

[63] J.P. Hirth, J. Lothe, Theory of Dislocations, second ed., Krieger Publishing Company, Virginia, 1982.

[64] B. Gurrutxaga-Lerma, D.S. Balint, D. Dini, D.E. Eakins, A.P. Sutton, A dynamic discrete dislocation plasticity method for the simulation of plastic relaxation under shock loading, Proc. R. Soc. A Math. Phys. Eng. Sci. 469 (2013) 20130141.

[65] M.A. Shehadeh, E.M. Bringa, H.M. Zbib, J.M. McNaney, B.A. Remington, Simulation of shock-induced plasticity including homogeneous and heterogeneous dislocation nucleations, Appl. Phys. Lett. 89 (2006) 10.

[66] O.M.D.M. Messé, S. Stekovic, M.C. Hardy, C.M.F. Rae, Characterization of plastic deformation induced by shot-peening in a Ni-base superalloy, JOM 66 (2014) 2502.

[67] J. Gil Sevillano, P. van Houtte, E. Aernoudt, Large strain work hardening and textures, Prog. Mater. Sci. 25 (1980) 69.

[68] Q. Yu, Z.-W. Shan, J. Li, X. Huang, L. Xiao, J. Sun, E. Ma, Strong crystal size effect on deformation twinning, Nature 463 (2010) 335.

[69] H. Abdolvand, M.R. Daymond, Multi-scale modeling and experimental study of twin inception and propagation in hexagonal close-packed materials using a crystal plasticity finite element approach; part II: local behavior, J. Mech. Phys. Solids 61 (2013) 803.